INTERNATIONAL JOURNAL FOR NUMERICAL METHODS IN FLUIDS, VOL. 19, 765–794 (1994)

# COMPUTATION OF UNSTEADY LAMINAR VISCOUS FLOW PAST AN AEROFOIL USING THE CPI METHOD

G. B. DENG, E. GUILMINEAU, J. PIQUET, P. QUEUTEY AND M. VISONNEAU
*CFD Group, LMF/URA 1217 CNRS, ECN, 1 Rue de la Noe, F-44072 Nantes Cedex, France*

## SUMMARY

The present work is a discussion of the computation of unsteady laminar incompressible two-dimensional viscous flow past complex geometries. A new physically consistent method is presented for the reconstruction of velocity fluxes which arise from the mass and momentum balance discrete equations. This closure method for fluxes makes possible the use of a cell-centred grid in which velocity and pressure unknowns share the same location while circumventing the occurrence of spurious pressure modes. The method is validated using the impulsively started cylinder problem for circular or aerofoil-like shapes at several Reynolds numbers of the order of $10^3$–$10^4$.

KEY WORDS Laminar viscous flow CPI method Aerofoil

## 1. INTRODUCTION

One of the most important CFD topics is the computation of unsteady incompressible flow in complex geometry using curvilinear co-ordinate systems. Although considerable progress in numerical methods has been made in the last decade, the present state of the art is still unsatisfactory. For incompressible flows problems occur in relation to the pressure field when the primitive variable formulation is used. Given an initial divergence-free velocity field, the primary role of pressure is to keep this velocity field divergence-free, while this pressure does not explicitly appear in the divergence-free condition. The governing equation for pressure is usually derived from the momentum equation if we require incompressibility. The solution of this equation is not straightforward and is the most time-consuming part of the algorithm.

In the present paper a new finite volume cell-centred two-step method is considered using the Cartesian velocity components and the pressure as dependent variables. A collocated grid is used in which all dependent variables are stored at the same locations. It is well known that a difficulty is usually generated by such a collocated approach, namely the possibility of spurious pressure oscillations caused by a null space in the matrix associated with the discrete Poisson equation for pressure.[1] To guarantee the existence of a unique solution for pressure, it is necessary to satisfy the integral compatibility constraint associated with the non-definite character of the pressure problem[2,3] (one of the eigenvalues of the pressure problem is zero and the pressure solution is unique within an arbitrary constant). On curvilinear grids it is well known that the use of a staggered mesh[4] does not forbid the occurrence of pressure oscillations by default unless contravariant velocity components are used as dependent variables.[5,6] Owing to its reduced storage requirements and simplicity of programming, the use of a collocated grid is thus preferred. Since the Cartesian velocity components are retained as dependent variables, the mass fluxes

CCC 0271–2091/94/210765–30

*Received November 1993*
*Revised January 1994*

involved in the integral form of the continuity equation are not available as dependent variables and consequently must be interpolated. This is the so-called flux reconstruction problem which requires the construction of an interpolation operator $\mathcal{M}$ and this will be dealt with in Section 3.2. The flux reconstruction must satisfy accuracy and monotonicity requirements while avoiding spurious pressure modes. A major breakthrough in this respect is due to Rhie and Chow.[7] These authors write a flux reconstruction at the interface which mimics a momentum equation: the pressure gradient is discretized at the interface while the remaining part of the momentum equation is interpolated. The resulting flux is used only in the continuity equation and this prevents the occurrence of spurious pressure modes. However, although the approach provides a satisfactory solution for the discretization of the continuity equation, the momentum equation is not concerned. In order to reconstruct the fluxes in a more systematic way, Schneider and Raw[8] deduce the flux reconstruction formulae from discretized momentum equations written on staggered grids and use the reconstructed fluxes in the discrete continuity equation as well as in the momentum equation. The present method, called CPI (consistent physical interpolation), shares this main idea with Reference 8 but departs from it in several characteristic features which will be discussed in Section 3.3. Its name stems from the fact that the fluxes are reconstructed explicitly from a momentum equation which is consistent with the physics (in contrast with Reference 8) while involving a more compact stencil than Reference 7. The present method, like References 7 and 8, belongs to the class of null-space-free methods[9] in that the interpolation operator $\mathcal{M}$ between the nodal velocity field $\mathbf{U}$ and the flux field $\mathbf{u} = \mathcal{M}\mathbf{U}$ at cell faces can be seen as generating an approximate projection method in which the velocity field $\mathbf{U}$ itself is necessarily[3] not solenoidal cell-by-cell, but only in some approximate sense, while the interpolated flux field $\mathbf{u}$ is exactly cell-by-cell solenoidal.

The CPI method will be detailed in the general case of curvilinear co-ordinates and the results obtained will be validated in Section 4 by studying the unsteady flow past an impulsively started cylinder of circular or aerofoil-like shape. Besides being physically interesting, such problems have often been used as numerical test cases for unsteady flow studies involving massive separation. Moreover, for these cases significant detailed experiments at relatively low Reynolds numbers are available.

## 2. THE EQUATIONS

The unsteady incompressible Navier–Stokes equations can be written as

$$\nabla \cdot \mathbf{U} = 0, \tag{1}$$

$$\frac{\partial \mathbf{U}}{\partial t} + \nabla \cdot \mathbf{F} = 0, \tag{2}$$

where the Cartesian components $\bar{F}_{kj}$ of the momentum flux $\mathbf{F}$ are given by

$$\bar{F}_{kj} = \bar{U}_j \bar{U}_k + P\delta_{kj} - \frac{1}{Re}\frac{\partial \bar{U}_k}{\partial x_j}. \tag{3}$$

They involve the Cartesian velocity components $\{\bar{U}_k\}$, the pressure $P$, the Reynolds number $Re = U_\infty L/\nu$, where $L$ is the aerofoil chord (or cylinder diameter), $U_\infty$ is the freestream velocity and $\nu$ is the kinematic viscosity of the fluid, and the Kronecker symbol $\delta_{kj}$. From now on the summation convention over repeated italic indices is used unless otherwise specified.

For applications to be considered, the complexity of the geometry prevents the use of Cartesian

co-ordinates. Numerical co-ordinate transformations are required in order to facilitate the application of boundary conditions and transform the physical domain $\Omega$ in which the flow is studied into a rectangular domain $\{\xi^1, \xi^2, \xi^3\}$. This computational domain consists of a set of stacked unit cubes of sides $\Delta\xi^i = 1$, $i = 1, 2, 3$. Each unit cube in the computational plane is a curvilinear hexahedron in the physical plane, the sides of which are measured by the moduli of the covariant vectors $\mathbf{a}_i = \partial\mathbf{R}/\partial\xi^i$. The transformation involves byproducts from the covariant basis. Of particular interest are (i) the area vectors $\mathbf{b}^i = \mathbf{a}_j \times \mathbf{a}_k$ ($i, j, k$ in cyclic order) which measure the oriented area of a small surface of unit sides along $\xi^j$ and $\xi^k$ on a $\xi^i$ = const. surface in the computational space, where $\mathbf{b}^i$ is constructed from two small triangle-like surfaces in the physical space; (ii) the Jacobian $J$ of the transformation from the computational space of the co-ordinates $\{\xi^i\}$ to the physical space of the Cartesian co-ordinates $\{x_i\}$, which measures the 'physical' volume of a unit cube in the computational space and is evaluated in such a way that $\mathbf{a}_i \cdot \mathbf{b}^j = J\delta_i^j$—this parallelepiped appears as a hexahedron-like volume in the physical space; (iii) the covariant and contravariant metric tensors $g_{ij} = \mathbf{a}_i \cdot \mathbf{a}_j$ and $g^{ij} = g^{-1}\mathbf{b}^i \cdot \mathbf{b}^j$, where $g$, the determinant of $g_{ij}$, is the square $J^2$ of the previously defined Jacobian.

Using the chain rule derivative formula $\partial\xi^k/\partial x_i = J^{-1}b_i^k$, we obtain

$$\nabla \cdot \mathbf{U} = J^{-1}\frac{\partial(JU^i)}{\partial\xi^i} = J^{-1}\frac{\partial(b_k^i\bar{U}_k)}{\partial\xi^i}. \tag{4}$$

If $\bar{U}_i = \delta_k^i$ with $k = 1, 2, 3$, equation (4) yields the so-called first geometric conservation law which can be expressed as follows: when properly discretized, areas of a discrete cell will sum to the total volume. The momentum equation (2) is written in the strong conservation form

$$\frac{\partial\bar{U}_k}{\partial t} + \frac{1}{J}\frac{\partial(b_j^i\bar{F}_{kj})}{\partial\xi^i} = 0,$$

$$\bar{F}_{kj} = \bar{U}_j\bar{U}_k + P\delta_{kj} - \frac{a_j^m}{Re}\frac{\partial\bar{U}_k}{\partial\xi^m}. \tag{6}$$

The convective form

$$\frac{\partial\bar{U}_k}{\partial t} + \left(U^i - \frac{f^i}{Re}\right)\frac{\partial\bar{U}_k}{\partial\xi^i} + a_i^k\frac{\partial P}{\partial\xi^m} = \frac{g^{im}}{Re}\frac{\partial^2\bar{U}_k}{\partial\xi^i\partial\xi^m} \tag{7}$$

will also prove necessary in the sequel, where the so-called stretching functions $f^i$ are defined by

$$f^i = \frac{1}{J}\frac{\partial}{\partial\xi^m}\left(\frac{\mathbf{b}^i \cdot \mathbf{b}^m}{J}\right). \tag{8}$$

## 3. THE NUMERICS

### *3.1. Grid lay-out and discrete equations*

The so-called collocated cell-centred grid lay-out is used: the Cartesian velocity components and the pressure share the same location at the centre of the control volume (Figure 1). Owing to its non-standard character, it is useful to make notation conventions explicit, restricting ourselves to two-dimensional problems. Neighbours of the point NN at the centre of the control

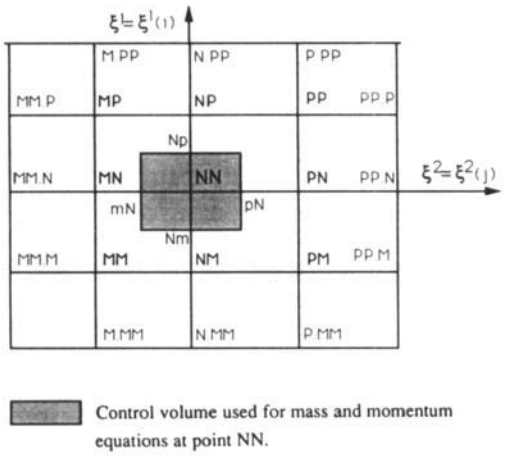


Figure 1. Schematic sketch of presently used notations

volume $D$ are identified by two uppercase letters: the first is relative to the direction $\xi^1$, the second to the direction $\xi^2$. Points are identified with the letter M (minus one), P (plus one) or N (null). The fluxes $JU^i$ involving the contravariant velocity components $U^i$ are located on the faces of the control volume (identified by a lowercase letter) in the direction of the normal to the face. Grid points are located at vertices of the control volume. In the following $\bar{U}_k(\mathrm{NN})$ will be the unknown $k$th Cartesian velocity component at point NN. The flux at cell interface pN is identified as $(JU^i)(\mathrm{pN})$. Although non-standard, the present notation allows a straightforward coding of the method, particularly in the three-dimensional case.

The discrete divergence of the flux $\Phi$ over the control volume $D$ is simply

$$(\Delta_i \Phi^i)(\mathrm{NN}) = \Phi^1(\mathrm{pN}) - \Phi^1(\mathrm{mN}) + \Phi^2(\mathrm{Np}) - \Phi^2(\mathrm{Nm}), \tag{9}$$

so that the discrete continuity equation results from $\Phi = J\mathbf{U}$.

The time derivative is discretized using a second-order-accurate backward Euler method involving the time levels $t^0 \equiv t - \Delta t$ and $t^{00} \equiv t - 2\Delta t$ besides the actual time level $t$. We then have

$$\frac{\partial \phi}{\partial t} \approx e_1 \Phi + e_0 \Phi^0 + e_{00} \Phi^{00},$$

with

$$\Phi \approx \phi(t), \qquad \Phi^0 \approx \phi(t^0), \qquad \Phi^{00} \approx \phi(t^{00}), \tag{10}$$

Using (9) and (10) yields the motion equations

$$J^{-1}(\mathrm{NN})\Delta_i(b_j^i \bar{U}_j)(\mathrm{NN}) = 0, \tag{11}$$

$$e_1 \bar{U}_k(\mathrm{NN}) + [e_0 \bar{U}_k^0(\mathrm{NN}) + e_{00} \bar{U}_k^{00}(\mathrm{NN})] + \frac{1}{J(\mathrm{NN})} \Delta_i(b_j^i \bar{F}_{kj})(\mathrm{NN}) = 0. \tag{12}$$

In the discrete divergence at point NN in (12) the linearized momentum flux $\mathbf{b}^i \cdot \bar{\mathbf{F}}_k$ is defined at interfaces pN, mN, Np and Nm as indicated in (9). For instance,

$$(\mathbf{b}^i \cdot \bar{\mathbf{F}}_k)(\mathrm{pN}) = \left((\mathbf{b}^i \cdot \mathbf{U}^*)\bar{U}_k + Pb_k^i - \frac{\mathbf{b}^i \cdot \mathbf{a}^m}{Re}\frac{\partial \bar{U}_k}{\partial \xi^m}\right)(\mathrm{pN}), \tag{13}$$

where $\mathbf{U}^*$ is a prediction of the velocity field at the actual time. An iterative procedure is thus required at time $t$ in order to update $\mathbf{U}^*$, starting with $\mathbf{U}^* = \mathbf{U}^0$. The approximation of (13) and of similar fluxes at mN, Np and Nm is carried out using a centred scheme. For instance, with $i = 1$,

$$\begin{aligned}(\mathbf{b}^i \cdot \bar{\mathbf{F}}_k)(\mathrm{pN}) \approx\ & c_1(\mathrm{pN})\bar{U}_k(\mathrm{pN}) + \tfrac{1}{2}b_k^1(\mathrm{pN})[P(\mathrm{PN}) + P(\mathrm{NN})] - d_{11}(\mathrm{pN})[\bar{U}_k(\mathrm{pN}) - \bar{U}_k(\mathrm{NN})] \\ & - \tfrac{1}{4}d_{12}(\mathrm{pN})[\bar{U}_k(\mathrm{PP}) + \bar{U}_k(\mathrm{NP}) - \bar{U}_k(\mathrm{PM}) - \bar{U}_k(\mathrm{NM})],\end{aligned} \tag{14}$$

where $c_i = \mathbf{b}^i \cdot \mathbf{U}^*$ and $d_{im} = \mathbf{b}^i \cdot \mathbf{a}_m/Re$ are evaluated at pN for $i = 1, 2$. Similar expressions are obtained at other face points mN, Np and Nm.

### *3.2. The reconstruction problem and its formal solution*

It appears that besides unknown nodal values of the Cartesian velocity components, expressions such as (14) involve the values $\bar{U}_k(\mathrm{pN})$ which are also unknown, *but at points which are not nodal points.* This introduces the so-called *reconstruction problem*: fluxes such as $\bar{U}_k(\mathrm{pN})$ which are not defined at nodal points must be expressed in terms of nodal unknowns. The interpolation procedure which solves the reconstruction problem must avoid spurious pressure modes which may exist when collocated grids are used. One of the most efficient ways to overcome this difficulty is to use a physical interpolation approach in which a velocity integration point value such as $\bar{U}_k(\mathrm{pN})$ is expressed not only in terms of values of $\bar{U}_k$ at the neighbouring nodes of pN, the set of which (Figure 1) is denoted $NB(\mathrm{pN}) = \{\mathrm{NN}, \mathrm{PN}, \mathrm{MN}, \mathrm{PP}, \mathrm{NP}, \mathrm{NM}\}$, but also in terms of values of other velocity components and pressure at $NB(\mathrm{pN})$. The most classical approach is the Rhie and Chow interpolation,[7] where $\bar{U}_k(\mathrm{pN})$ involves besides $NB(\mathrm{pN})$ the nodes PP.P, PP.N and PP.M (Figure 2(a)). Another interpolation, due to Schneider and

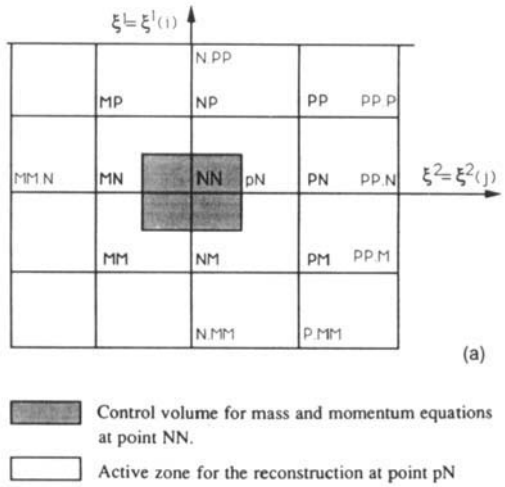


Figure 2(a). The Rhie and Chow influence stencil of point NN

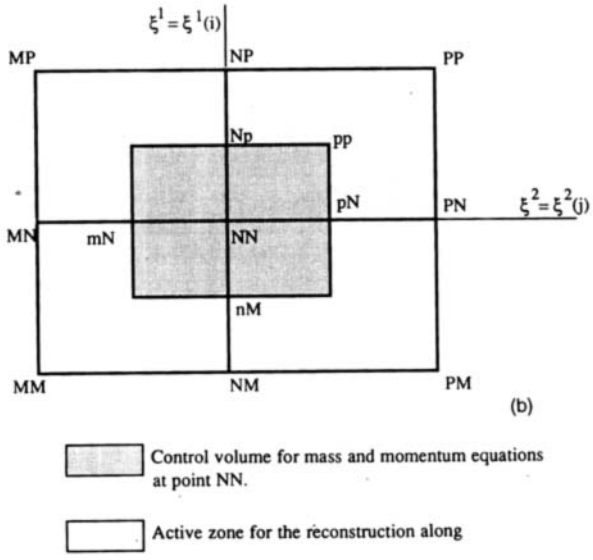


Figure 2(b). The Schneider and Raw influence stencil of point NN

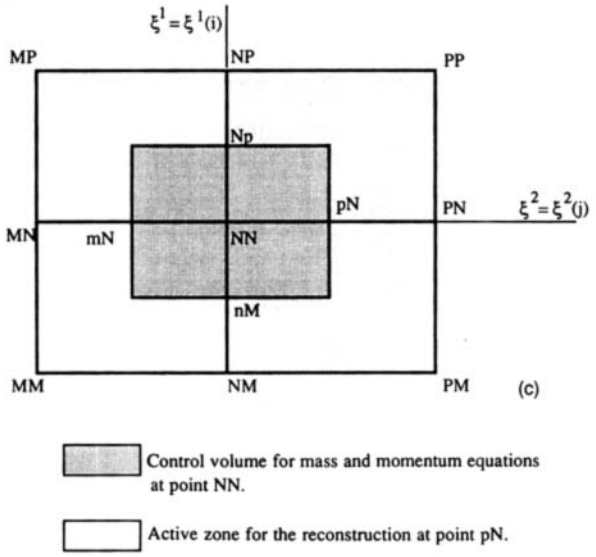


Figure 2(c). The influence stencil of point NN for the CPI method

Raw,[8] involves several integration point values (Figure 2(b)) for the set $NB(\mathrm{pN})$. In the following we present the consistent physical interpolation (CPI) which determines $\bar{U}_k(\mathrm{pN})$ from the solution of the convective form of the momentum equations at point pN. This interpolation involves the set of neighbours $NB(\mathrm{pN})$ of influencing nodes (Figure 2(c)). The result can be written at pN as

$$(e_1 + D_{\mathrm{pN}})\bar{U}_k(\mathrm{pN}) = \sum_{NB(\mathrm{pN})} C^{U}_{NB(\mathrm{pN})}\bar{U}_k[NB(\mathrm{pN})] + \sum_{NB(\mathrm{pN})} {}^{CPk}_{NB(\mathrm{pN})}P[NB(\mathrm{pN})] + S_k(\mathrm{pN}) \quad (15)$$

and in a similar way at mN, Np and Nm. Equation (15) indicates that integration point values $\bar{U}_k(\mathrm{pN})$ are given by an *explicit formula*, in contrast with the closure of Reference 8 which requires the inversion of a 4 × 4 system. For the other interfaces of the control volume $D$ the sets of active neighbours are

$$NB(\mathrm{mN}) = \{\mathrm{MN}, \mathrm{NN}, \mathrm{MP}, \mathrm{NP}, \mathrm{MM}, \mathrm{MN}\},$$
$$NB(\mathrm{Np}) = \{\mathrm{NN}, \mathrm{NP}, \mathrm{NM}, \mathrm{PM}, \mathrm{PN}, \mathrm{PP}\},$$
$$NB(\mathrm{Nm}) = \{\mathrm{NN}, \mathrm{PN}, \mathrm{MN}, \mathrm{PM}, \mathrm{NM}, \mathrm{MM}\}.$$

The influence coefficients satisfy the consistency conditions

$$\sum_{NB(\mathrm{pN})} C^U_{NB(\mathrm{pN})} = D_{\mathrm{pN}}, \qquad \sum_{NB(\mathrm{pN})} C^{Pk}_{NB(\mathrm{pN})} = 0, \quad k = 1, 2. \tag{16a,b}$$

The former relation (16a) indicates that $\bar{U}_k(\mathrm{pN})$ involves a weighted interpolation of $\bar{U}_k$ at neighbouring nodal values. The latter relation (16b) corresponds to the fact that the summation over pressure values is of the gradient type. It can be shown that on a uniform Cartesian grid the present interpolation formula is second-order-accurate compared with Reference 8 because of the treatment of the diffusion term in Reference 8. We shall need the generalized form

$$(e_1 + D_f)\bar{U}_k(f) = \sum_{NB(f)} C^U_{NB(f)} \bar{U}_k[NB(f)] + \sum_{NB(f)} C^{Pk}_{NB(f)} P[NB(f)] + S_k(f), \; f = \mathrm{pN}, \mathrm{mN}, \mathrm{Np}, \mathrm{Nm}, \tag{15'}$$

in the sequel. Equation (15') can be viewed as a definition of the so-called pseudovelocity

$$\hat{U}_k(f) = \frac{1}{e_1 + D_f}\left(\sum_{NB(f)} C^U_{NB(f)} \bar{U}_k[NB(f)] + S_k(f)\right) \tag{17a}$$

such that

$$\bar{U}_k(f) = \hat{U}_k(f) + \frac{1}{e_1 + D_f}\left(\sum_{NB(f)} C^{Pk}_{NB(f)} P[NB(f)\right). \tag{17b}$$

### *3.3. The CPI method using an exponential or a hybrid discretization*

We still have to demonstrate how the expression of the influence coefficients $C^U$ and $C^{Pk}$ and of the source term $S_k$ in (16) can be obtained from a discrete scheme for the momentum equation written at $f$ = pN, mN, Np, Nm. This will now be explained for the fluxes at point pN using the momentum equation written at pN.

The multiexponential scheme consists of using an exponential scheme in both directions. Let us consider the differential equation along, say, $\xi = \xi^1$:

$$d\frac{\partial^2 U}{\partial \xi^2} = c\frac{\partial U}{\partial \xi} + S. \tag{18}$$

The corresponding exponential scheme on a uniform grid of spacing $h$ is

$$C_{\mathrm{M}} U_{\mathrm{M}} + C_{\mathrm{N}} U_{\mathrm{N}} + C_{\mathrm{P}} U_{\mathrm{P}} = S_{\mathrm{N}},$$

with

$$C_P = \frac{c}{e^\gamma - 1}, \qquad C_M = \frac{ce^\gamma}{e^\gamma - 1}, \qquad C_N + C_M + C_P = 0. \tag{19}$$

This involves the mesh Peclet number $\gamma = ch/d$. The exponential scheme can be applied in each direction to equation (7) using mesh Peclet numbers $\gamma_1 = c_1 h_1/d_{11}$ and $\gamma_2 = c_2 h_2/d_{22}$. (Notice that on curvilinear grids the spacings $h_1$ and $h_2$ along $\xi^1$ and $\xi^2$ can be taken equal to 1, except close to the boundaries where they may take the value $\frac{1}{2}$.) The result written at pN is

$$\begin{aligned}(e_1 + C_{N1} + C_{N2})\bar{U}_k(\mathrm{pN}) + C_{P1}\bar{U}_k(\mathrm{PN}) + C_{M1}\bar{U}_k(\mathrm{NN}) + \tfrac{1}{2}C_{P2}[\bar{U}_k(\mathrm{NP}) + \bar{U}_k(\mathrm{PP})] \\ + \tfrac{1}{2}C_{M2}[\bar{U}_k(\mathrm{NM}) + \bar{U}_k(\mathrm{PM})] \\ = \left[-\left(d_{im}\frac{\partial^2 \bar{U}_k}{\partial\xi^i \partial\xi^m}\right)_{i\neq m} + a_k^i \frac{\partial P}{\partial \xi^i}\right](\mathrm{pN}) - e_0 \bar{U}_k^0(\mathrm{pN}) - e_{00}\bar{U}_k^{00}(\mathrm{pN}),\end{aligned} \tag{20}$$

where the influence coefficients at pN are deduced from (19) as

$$C_{Pi} = \frac{c_i}{e^{\gamma_i} - 1}, \qquad C_{Mi} = \frac{c_i e^{\gamma_i}}{e^{\gamma_i} - 1}, \qquad C_{Ni} + C_{Mi} + C_{Pi} = 0,$$

with $i = 1, 2$. The second-order cross-derivatives in (20) are treated using a centred scheme:

$$\left[\left(d_{im}\frac{\partial^2 \bar{U}_k}{\partial\xi^i \partial\xi^m}\right)_{i\neq m}\right](\mathrm{pN}) \approx \frac{1}{4h_1 h_2} d_{12}(\mathrm{pN})[\bar{U}_k(\mathrm{PP}) - \bar{U}_k(\mathrm{NP}) - \bar{U}_k(\mathrm{PM}) + \bar{U}_k(\mathrm{NM})]. \tag{21}$$

Finally, the pressure gradient at pN in (20) is approximated as

$$a_k^1 \frac{\partial P}{\partial \xi^1}(\mathrm{pN}) \approx \frac{1}{2h_1} a_k^1(\mathrm{pN})[P(\mathrm{NP}) - P(\mathrm{NN})], \tag{22a}$$

$$a_k^2 \frac{\partial P}{\partial \xi^2}(\mathrm{pN}) \approx \frac{1}{4h_2} a_k^2(\mathrm{pN})[P(\mathrm{PP}) + P(\mathrm{NP}) - P(\mathrm{PM}) - P(\mathrm{NM})]. \tag{22b}$$

The resulting influence coefficients in (15) are obtained by substitution of (21) and (22) into (20). The result is given in Appendix I.

Instead of a multiexponential scheme, the closure for $\bar{U}_k(\mathrm{pN})$ may be obtained from a hybrid scheme corresponding to the discretization of the first-order derivative $\partial U/\partial\xi$ according to

$$\frac{\partial U}{\partial \xi} \equiv \alpha \frac{U(\mathrm{N}) - U(\mathrm{M})}{h} + (1 - \alpha)\frac{U(\mathrm{P}) - U(\mathrm{N})}{h} \tag{23}$$

The upwind parameter $\alpha$ is a function of the mesh Peclet number $\gamma$ and can be computed according to

$$\alpha = \frac{1 + (\gamma - 1)e^\gamma}{\gamma(e^\gamma - 1)}. \tag{24}$$

Then the reconstructed velocity at pN, $\bar{U}_k(\mathrm{pN})$, is given by

$$e_1\bar{U}_k(\mathrm{pN})+c_1\left(\alpha_1\frac{\bar{U}_k(\mathrm{pN})-\bar{U}_k(\mathrm{NN})}{h_1}+(1-\alpha_1)\frac{\bar{U}_k(\mathrm{PN})-\bar{U}_k(\mathrm{pN})}{h_1}\right)$$
$$+c_2\left(\alpha_2\frac{\bar{U}_k(\mathrm{pN})-[\bar{U}_k(\mathrm{NM})+\bar{U}_k(\mathrm{NM})]/2}{h_2}+(1-\alpha_2)\frac{[\bar{U}_k(\mathrm{NP})+\bar{U}_k(\mathrm{PP})]/2-\bar{U}_k(\mathrm{pN})}{h_2}\right.$$
$$=\left[-\left(d_{im}\frac{\partial^2\bar{U}_k}{\partial\xi^i\partial\xi^m}\right)+a_k^i\frac{\partial P}{\partial\xi^i}\right](\mathrm{pN})-e_0\bar{U}_k^0(\mathrm{pN})-e_{00}\bar{U}_k^{00}(\mathrm{pN}). \tag{25}$$

Using (22) and centred second-order derivatives yields again the influence coefficients in (15).

### *3.4. The equations for the nodal unknowns*

Upon substitution of closures (15′) written at pN, mN, nP and nM into the discrete momentum equation (12) where relations such as (13) and (14) have been accounted for, we obtain the following discrete scheme for the momentum equations corresponding to $k = 1, 2$:

$$[e_1 + D^U(\mathrm{NN})]\bar{U}_k(\mathrm{NN}) = \sum_{NB(\mathrm{NN})} K^U_{NB(\mathrm{NN})}\bar{U}_k[NB(\mathrm{NN})]$$
$$+\sum_{NB(\mathrm{NN})} K^{kP}_{NB(\mathrm{NN})}P[NB(\mathrm{NN})]+\Sigma_k(\mathrm{NN}), \tag{26}$$

where the velocity and pressure unknowns involved are located only at NN and at the eight nodal neighbours of the set $NB(\mathrm{NN}) = \{\mathrm{MM}, \mathrm{MN}, \mathrm{MP}, \mathrm{NM}, \mathrm{NP}, \mathrm{PM}, \mathrm{PN}, \mathrm{PP}\}$; the summations are over the eight corresponding contributions. The influence coefficients $K^{kP}_{NB(\mathrm{NN})}$ involved in the summation for the pressure terms result from the identity

$$\sum_{NB(\mathrm{NN})} K^{kP}_{NB(\mathrm{NN})}P[NB(\mathrm{NN})] = \frac{1}{J(\mathrm{NN})}\Delta_f\left(b_k^f P+\frac{c_f}{e_1+D_f}\sum_{NB(f)} C^{Pk}_{NB(f)}P[NB(f)]\right). \tag{27}$$

If the closures such as (15′) are substituted into the continuity equation (11), we obtain from a pressure equation of the form

$$\frac{1}{J(\mathrm{NN})}\Delta_f\left[\frac{b_k^f}{e_1+D_f}\left(\sum_{NB(f)} C^U_{NB(f)}\bar{U}_k[NB(f)]+\sum_{NB(f)} C^{Pk}_{NB(f)}P[NB(f)]+S_k(f)\right)\right]=0 \tag{28a}$$

the pressure discrete equation

$$\sum_{NB(\mathrm{NN})} K^{Pk}_{NB(\mathrm{NN})}\bar{U}_k[NB(\mathrm{NN})]+\sum_{NB(\mathrm{NN})} K^{PP}_{NB(\mathrm{NN})}P[NB(\mathrm{NN})]=\Sigma_P(\mathrm{NN}). \tag{28b}$$

The two momentum equations (26) (k = 1, 2) and equation (28b) written at each inner point NN$(i, j)$ in the computational space generate the system of unknowns. We group the three unknowns $\bar{U}_1$, $\bar{U}_2$, and $P$ at each grid point $(i, j)$ to define a vector $\mathbf{X}(i,j) \equiv \|\bar{U}_1(i,j)\ \bar{U}_2(i,j)\ P(i,j)\|^T$ with three components and we order the unknowns from values $i = 1$ to $i = i_{\max}$ and for any given value of $i$ from $j = 1$ to $j = j_{\max}$. When the $i(j-1)$th, $ij$th and $i(j+1)$th rows of the matrix **A** corresponding to (26) $(k = 1)$ (26), $(k = 2)$ and (28b) are also grouped in this order, the matrix **A** appears as a block 3 × 3 nine-diagonal matrix whose non-vanishing elements in the $ij$th block 3 × 3 row are located on the $(i-1)(j-1)$th, $(i-1)j$th, $(i-1)(j+1)$th columns (influence coefficients of points MM$(i,j)$, MN$(i,j)$, MP$(i,j)$ respectively),

on the $i(j-1)$th, $ij$th, $i(j+1)$th columns (influence coefficients of points NM$(i,j)$, NN$(i,j)$, NP$(i,j)$ respectively) and on the $(i+1)(j-1)$th, $(i+1)j$th, $(i+1)(j+1)$th columns (influence coefficients of points PM$(i,j)$, PN$(i,j)$, PP$(i,j)$ respectively). Appendix II presents the resulting matrix **A** and the detailed structure of a characteristic elementary block; this demonstrates the optimal compacity of the CPI method with respect to Reference 7.

Equation (28a) can be viewed as a pressure equation if the substituted closure takes the form of (16) instead of (15′):

$$\mathrm{div}(\nabla P) \equiv \frac{1}{J(\mathrm{NN})}\Delta_f\left(\frac{b_k^f}{e_1 + D_f}\sum_{NB(f)} C_{NB(f)}^{Pk} P[NB(f)]\right) = -\mathrm{div}\,\hat{\mathbf{U}} \equiv -\frac{1}{J(\mathrm{NN})}\Delta_f[b_k^f \hat{U}_k(f)]. \quad (29)$$

### *3.5. Pressure–velocity coupling algorithm*

The algorithm which yields a coupled solution of the system (26), (29) is directly inspired by the PISO algorithm;[10] it consists of the following steps.

1. Initialize the velocity field and the pressure field at $t = t^0$.
2. New time step $t = t + \Delta t$.
3. Start iterative procedure with $\bar{U}_k = \bar{U}_k^0$, $P = P^0$, $\bar{U}_k(f) = \bar{U}_k^0(f)$.
4. Compute the reconstruction coefficients from the field of step 3.
5. Solve the momentum equations to obtain a new prediction for $\bar{U}_k$.
6. Solve the continuity equation to obtain pressure $P$ with coefficients obtained from step 4 and $\bar{U}_k$ from step 5.
7. Correct the velocity field with coefficients from step 4, $\bar{U}_k$ from step 3 and $P$ from step 5.
8. Reconstruction at interfaces to get $\bar{U}_k(f)$ with coefficients from step 4, $P$ from step 6 and $\bar{U}_k$ from step 7.
9. If non-linear residuals are low enough, go to step 1 and update $t$; otherwise, go to step 3 and update the iteration count within time step $t$.

## 4. RESULTS

### *4.1. Introduction*

As already mentioned in Section 1, the CPI method is validated using the impulsively started cylinder problem. The cylinder is circular or aerofoil-shaped. The former test case has been computed in detail in References 11 and 12 using the streamfunction–vorticity formulation. The results of the calculations were tested against experiments[13] for two moderately high Reynolds numbers for which the flow is laminar, namely $Re = 3000$ and 9500. The latter test case adds the complexity of a sharp trailing edge. An NACA 0012 shape is used, which makes it possible to carry out a detailed study of the dynamic stall over the aerofoil as a result of the massive separation which develops along the upper surface of the aerofoil. This geometry has often been calculated using the vorticity–streamfunction formulation, for the impulsive gust case as well as for superimposed pitching motions of the aerofoil,[15–21] or the velocity–vorticity formulation.[22–24]

The primitive variable formulation has not been considered as often, although it is better suited to turbulent models incorporated in the unsteady simulation.[25–28] For incompressible flows suitable finite difference or finite volume methods have been proposed,[7,27–29] while some finite element simulations are also available now.[30]

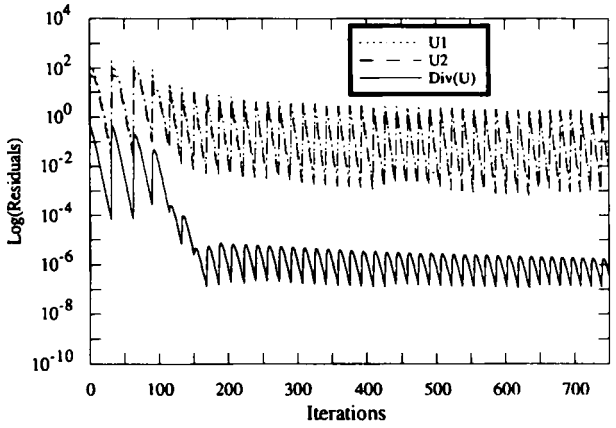


Figure 3. Evolution with time of non-linear residuals of momentum equations and continuity equation for exponential reconstruction. Impulsive start of circular cylinder at $Re = 3000$, mesh 120 × 100. Notice that $\bar{U}_1$ and $\bar{U}_2$ residuals can hardly be distinguished

In the present calculations a constant non-dimensional time step $\Delta t = 0{\cdot}01$ is used starting from a unit uniform flow field. At each time step the non-linear residuals are decreased by three orders of magnitude. This is considered to be sufficient insofar as we focus on results relative to the onset of the flow development to be compared with experimental data.[31,32]

### *4.2. Impulsively started circular cylinder*

*Case 1 ($Re = 3000$).* Figures 3 and 4 present the evolution with time of the residuals of the (momentum) equations for $\bar{U}_1$ and $\bar{U}_2$ and of the mass equation for $\nabla \cdot \mathbf{U}$. Such figures result from the two different schemes used for the flux reconstruction, namely the exponential (Figure 3) and hybrid (Figure 4) schemes. Each local maximum indicates the converged result at each time step of non-linear iterations. For each time step 15–25 non-linear iterations are

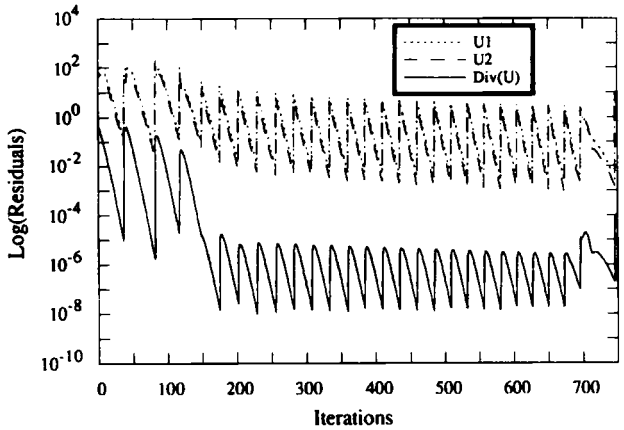


Figure 4. Evolution with time of non-linear residuals of momentum equations and continuity equation for hybrid reconstruction. Impulsive start of circular cylinder at $Re = 3000$, mesh 120 × 100. Notice that $\bar{U}_1$ and $\bar{U}_2$ residuals can hardly be distinguished

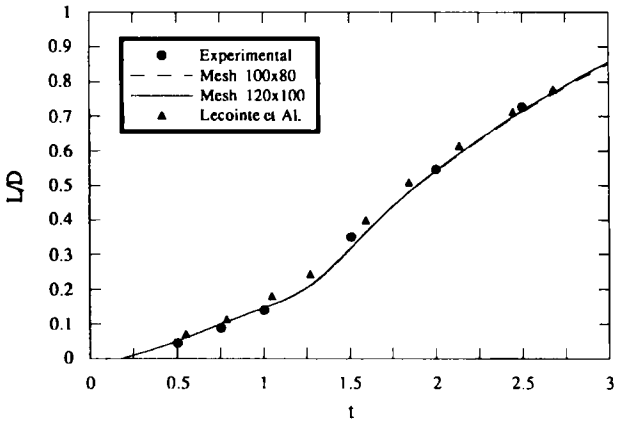


Figure 5. Impulsive start of circular cylinder at $Re = 3000$. Evolution with time of recirculation length normalized with cylinder diameter. Exponential reconstruction

used to lower the residuals by three orders of magnitude for the momentum equations. For a given total number of iterations the number of computed time steps is higher with the exponential reconstruction than with the hybrid reconstruction. Also, the level of $\nabla \cdot \mathbf{U}$-residuals is lower with the hybrid reconstruction than with the exponential reconstruction, especially after 700 iterations, corresponding to $t \approx 0{\cdot}25$, at which the birth of the primary eddy occurs. The evolution with time of the recirculation length is presented in Figures 5 and 6 for the exponential and hybrid reconstructions respectively. Results which look very similar are in good agreement with experimental data[13] as well as with calculations[11] using the vorticity–streamfunction formulation. We notice that a slight grid dependence is present for the hybrid reconstruction scheme, in contrast with the grid-independent results using the exponential reconstruction scheme. The onset of the primary eddy is found slightly later than in the boundary layer theory which yields $t_s = 0{\cdot}175$: the exponential reconstruction scheme produces $0{\cdot}19 \leqslant t_s \leqslant 0{\cdot}20$ and

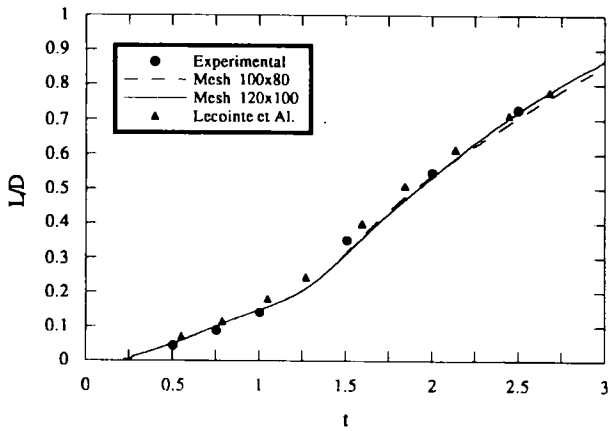


Figure 6. Impulsive start of circular cylinder at $Re = 3000$. Evolution with time of recirculation length normalized with cylinder diameter. Hybrid reconstruction

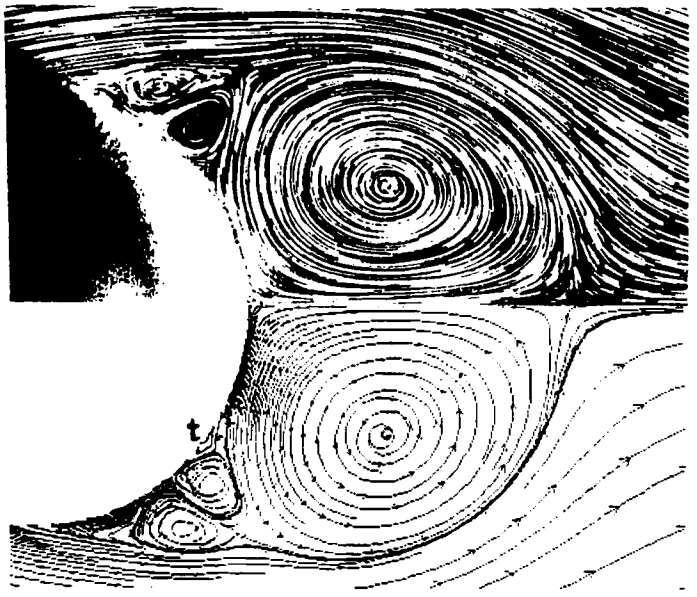

Figure 7. Impulsive start of circular cylinder at $Re = 3000$. Comparison of particle traces[13] (upper part) with computed streamlines (lower part) at $t = 2{\cdot}5$

the hybrid reconstruction scheme $0{\cdot}23 \leqslant t_s \leqslant 0{\cdot}24$. In both cases this is substantially later than in Reference 11, where a special procedure based on a Stokes solution is used immediately after the impulsive start. On the other hand, a consensus value of about 0·16 is usually claimed to be Reynolds-independent.[14] A secondary eddy appears at $t \approx 0{\cdot}91$, slightly later than in Reference 11 where $t \approx 0{\cdot}84$. A comparison at $t = 2{\cdot}5$ between computed streamlines and experimental path lines is provided in Figure 7. The agreement is good in view of the circumferential grid resolution: twin secondary eddies (the so-called $\alpha$-phenomenon) are located at $\theta_{E1} \approx 42°$ and $\theta_{E2} \approx 55°$, experimental values[13] are $\theta_{E1} \approx 43°$ and $\theta_{E2} \approx 54°$ and calculations[11] yield $\theta_{E1} \approx 45°$ and $\theta_{E2} \approx 56°$. Tertiary secondary eddies (t) appear also for $t \approx 2{\cdot}13$. The distribution of $\bar{U}_1$ along the symmetry axis of the wake is compared with experimental data[13] in Figures 8 and 9 using the exponential and hybrid reconstructions respectively. Again the sensitivity of solutions to the grid is low and a very slight discrepancy with experiments around $t = 2$ is apparent. Taken as a whole, the results appear very similar with both reconstructions and almost perfectly grid-independent, at least for the times considered.

*Case 2 (Re = 9500).* Since the same general conclusion results from the consideration of this case, we present only the results obtained with the hybrid reconstruction scheme on the finest grid. Figure 10 compares the recirculation length with experimental data[13] and with calculations.[11] The birth of the primary eddy occurs at about $t = 0{\cdot}20$; the secondary eddy appears at about $t \approx 0{\cdot}83$. For $t = 1{\cdot}75$ its location is $44° \leqslant \theta \leqslant 50$ °C, while calculations[11] yield $45° \leqslant \theta \leqslant 51°$. Experiments are compared with the results of the computation in Figure 11 for $t = 0{\cdot}75$, 1, 1·25 and 1·5, demonstrating the ability of the method to capture the $\beta$-phenomenon (maximum increase in the intensity of the primary eddy away from the axis) in spite of a slight underestimation of the intensity of the primary eddy.

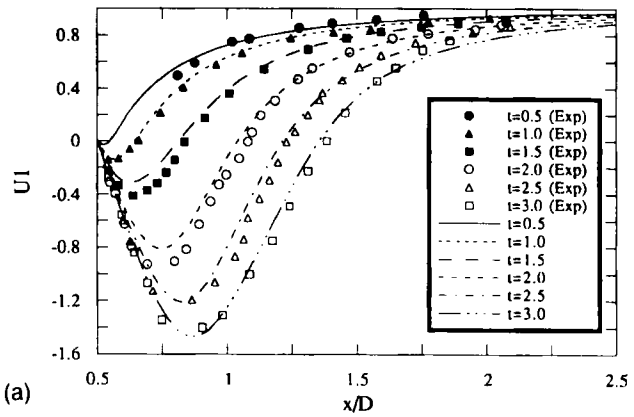


Figure 8(a). Impulsive start of circular cylinder at $Re = 3000$. Evolution with time of distribution of $\bar{U}_1$-velocity component along symmetry axis of wake. Exponential reconstruction scheme with 100 × 80 grid

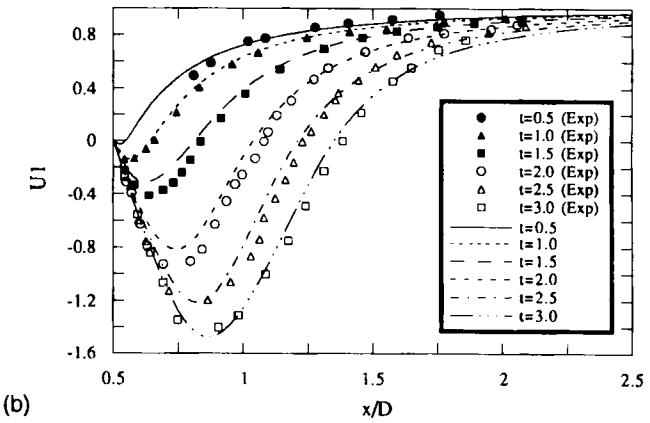


Figure 8(b). Impulsive start of circular cylinder at $Re = 3000$. Evolution with time of distribution of $U\bar{U}_1$-velocity component along symmetry axis of wake. Exponential reconstruction scheme with 120 × 100 grid

### *4.3. NACA 0012 aerofoil*

Again calculations have been carried out with the two reconstruction schemes for the fluxes using several grids (80 × 60, 90 × 100, 100 × 120—the second number gives the radial number of points). Insofar as the onset of the flow is studied, the results appear grid-independent. The analysis is focused on the 80 × 60 grid resulting from a Joukowski transformation similar to that used in References 13 and 14 and clustered close to the aerofoil (Figure 12(a)). The flux reconstruction uses the exponential scheme and the far-field boundary located at six chord lengths from the aerofoil. The first grid points away from the wall are located at 0·01 $L$ from the aerofoil. Two cases have been considered: Case 1—incidence 34 °, $Re = 1000$, impulsive start; Case 2—incidence 30 °, $Re = 3000$, impulsive start. For both cases experimental data are available.[29,30]

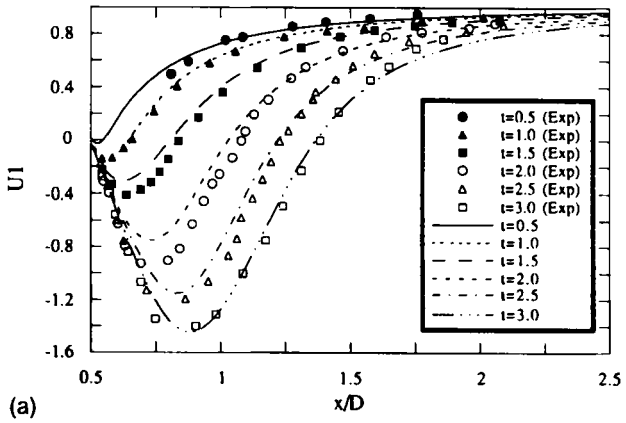


Figure 9(a). Impulsive start of circular cylinder at $Re = 3000$. Evolution with time of distribution of $\bar{U}_1$-velocity component along symmetry axis of wake. Hybrid reconstruction scheme with 100 × 80 grid

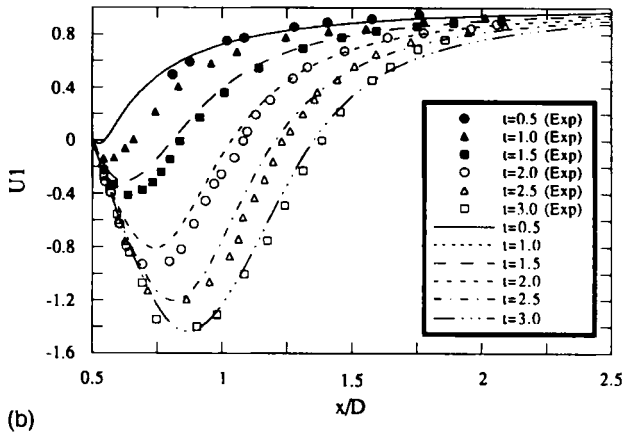


Figure 9(b). Impulsive start of circular cylinder at $Re = 3000$. Evolution with time of distribution of $\bar{U}_1$-velocity component along symmetry axis of wake. Hybrid reconstruction scheme with 120 × 100 grid

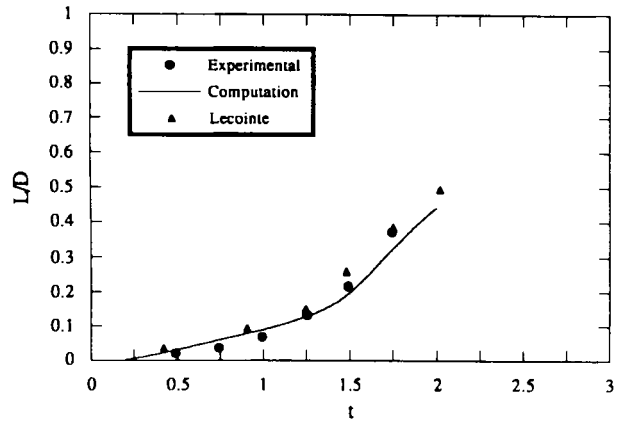


Figure 10. Impulsive start of circular cylinder at $Re = 9500$. Evolution with time of recirculation length normalized with cylinder diameter. Hybrid reconstruction with 120 × 100 mesh

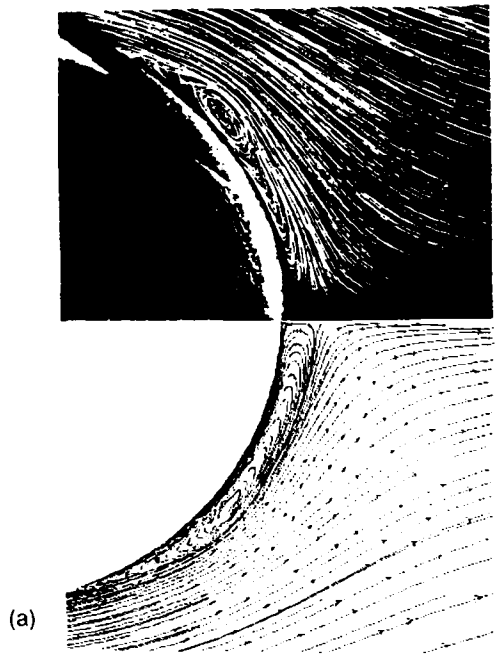


Figure 11(a). Impulsive start of circular cylinder at $Re = 9500$. Comparison of particle traces[13] (upper part) with computed streamlines (lower part) at $t = 0{\cdot}75$

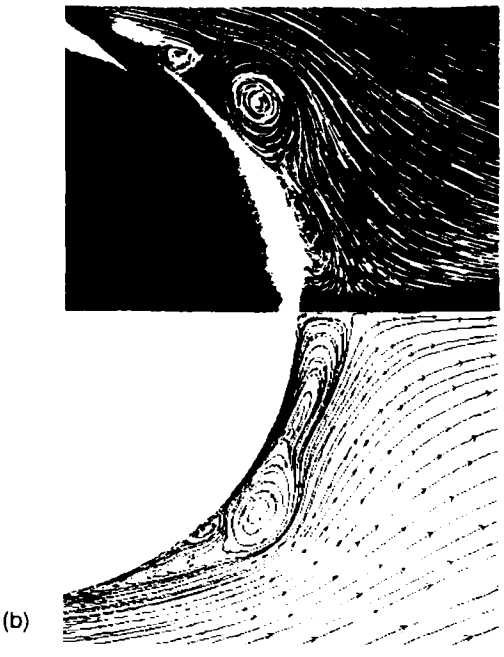


Figure 11(b). Impulsive start of circular cylinder at $Re = 9500$. Comparison of particle traces[13] (upper part) with computed streamlines (lower part) at $t = 1$

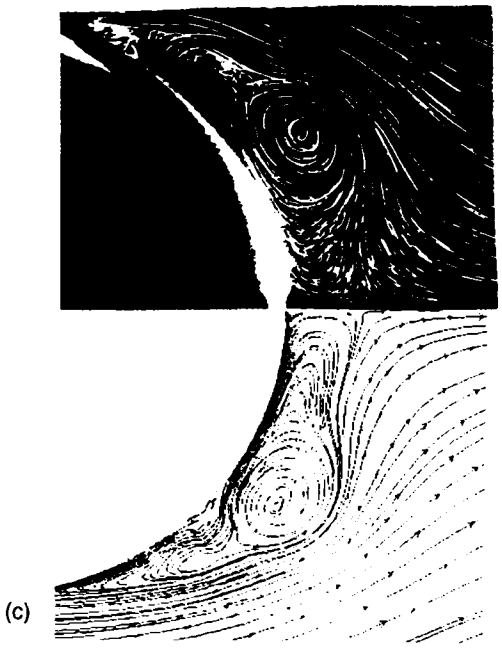


Figure 11(c). Impulsive start of circular cylinder at $Re = 9500$. Comparison of particle traces[13] (upper part) with computed streamlines (lower part) at $t = 1{\cdot}25$


Figure 11(d). Impulsive start of circular cylinder at $Re = 9500$. Comparison of particle traces[13] (upper part) with computed streamlines (lower part) at $t = 1{\cdot}5$

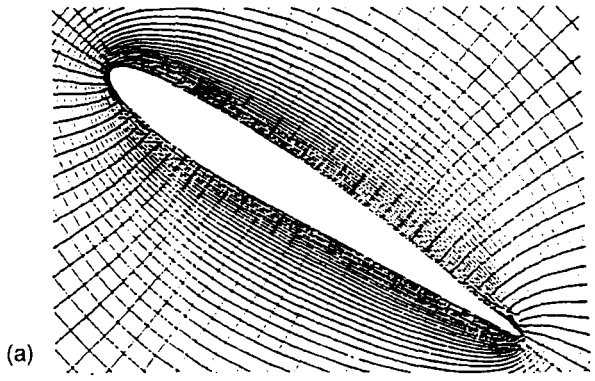

Figure 12(a). O-type grid used around NACA 0012 aerofoil

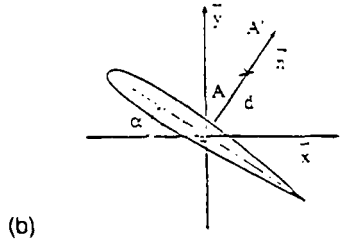


(b)

Figure 12(b). Schematic sketch of notations

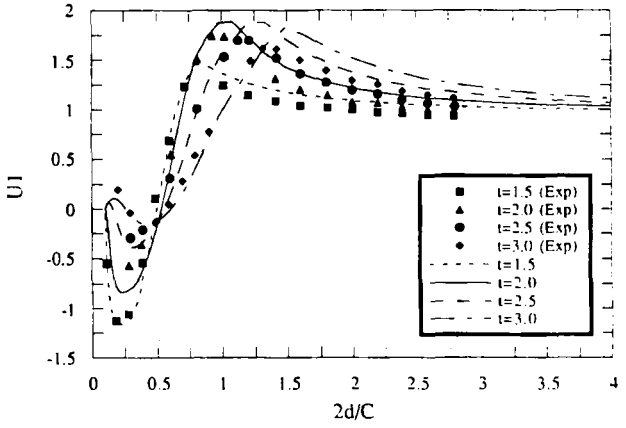


Figure 13. Impulsive start of aerofoil at $Re = 1000$, incidence 34°. Evolution with time of $\bar{U}_1$-velocity component along AA′ as a function of normalized distance to aerofoil

*Case 1.* Figure 13 shows the evolution of the velocity component $\bar{U}_1$ parallel to the direction of the oncoming flow with the distance to the aerofoil centre along AA′ (see Figure 12(b)). The calculation reproduces the overshooting velocity profile (Figure 13). However, the magnitude of the velocity is slightly overestimated with respect to the experimental data.

A comparison between calculations and experiments is provided in Figures 14–19 for the development of the stall phenomenon. For several times following the impulsive start we have

(a)

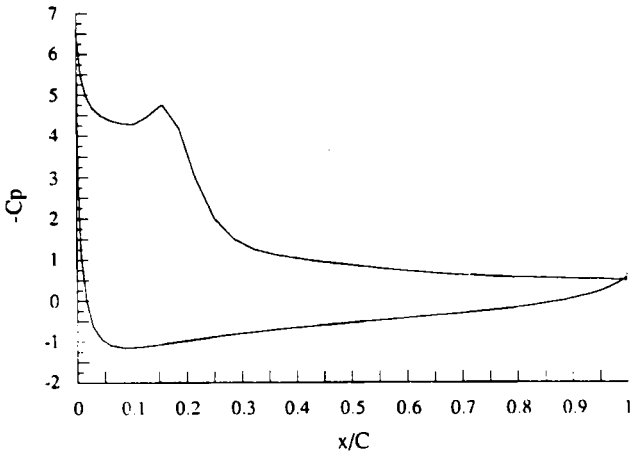


(c)

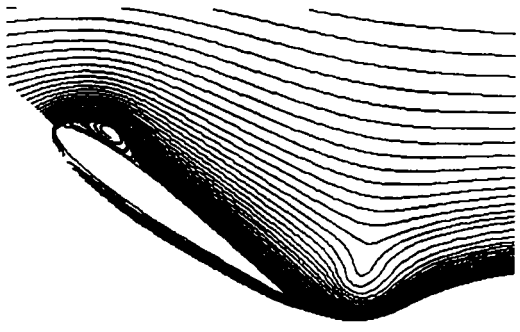

(b)

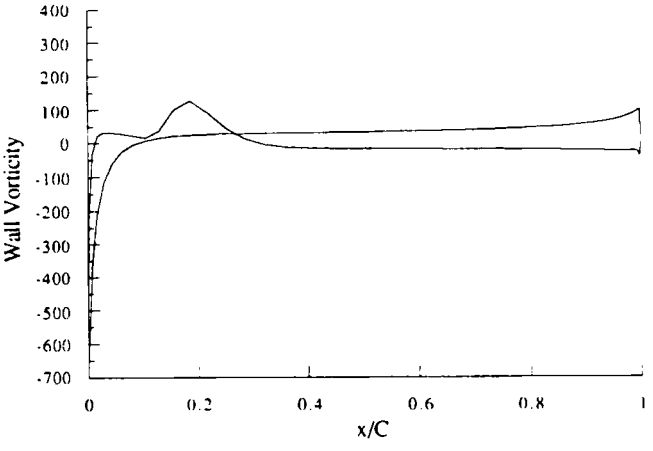


(d)

Figure 14. Impulsive start of aerofoil at $Re = 1000$, incidence 34 °, $t = 0{\cdot}4$: (a) visualization of path lines; (b) computed streamlines; (c) distribution of wall pressure coefficient; (d) wall vorticity distribution

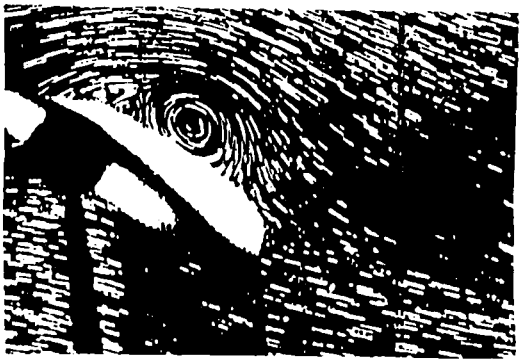

(a)

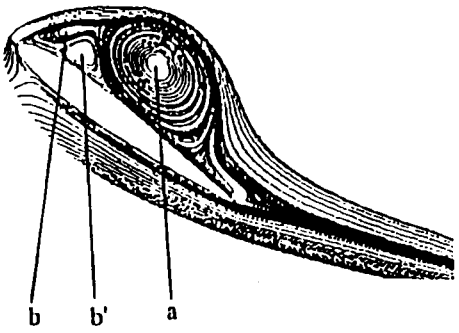


(b)

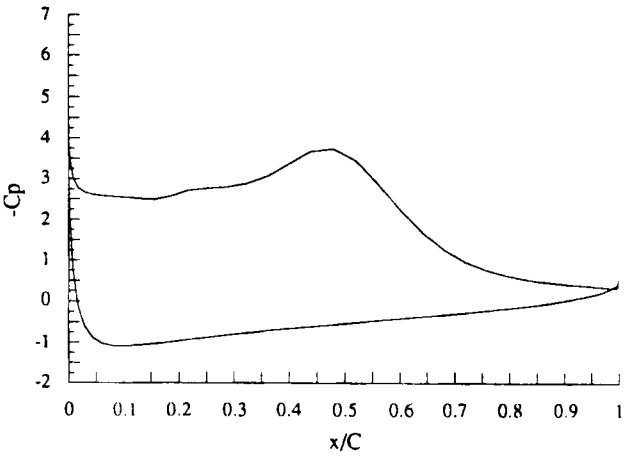


(c)

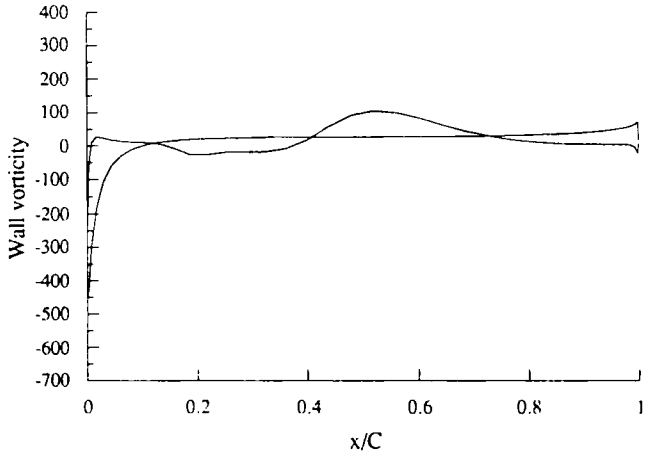


(d)

Figure 15. Impulsive start of aerofoil at $Re = 1000$, incidence 34 °, $t = 1{\cdot}6$: (a) visualization of path lines; (b) computed streamlines; (c) distribution of wall pressure coefficient; (d) wall vorticity distribution

(a)

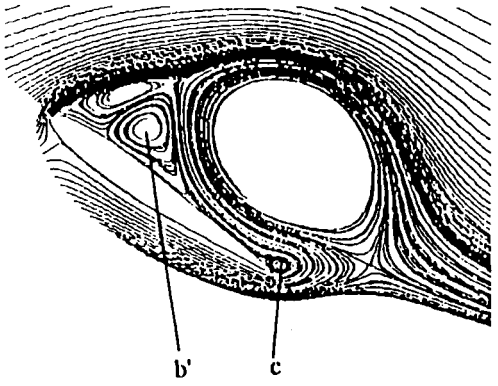


(b)

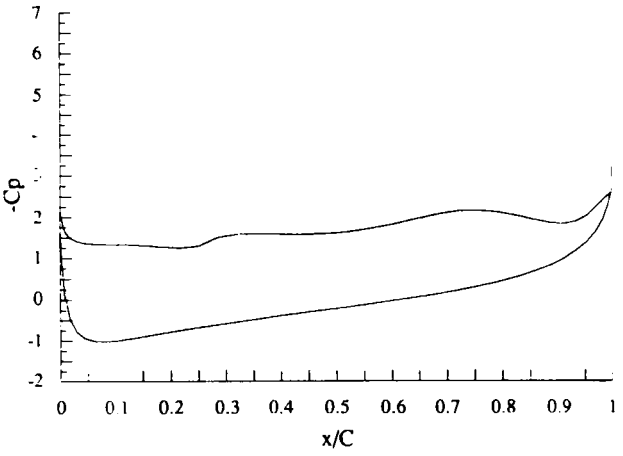


(c)

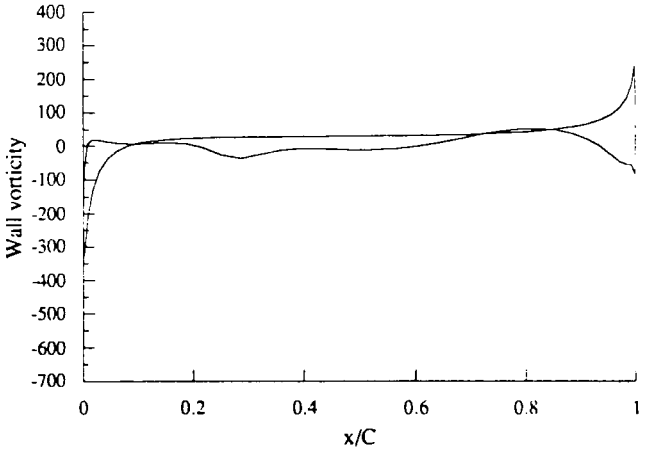


(d)

Figure 16. Impulsive start of aerofoil at $Re = 1000$, incidence 34 °, $t = 2{\cdot}8$: (a) visualization of path lines; (b) computed streamlines; (c) distribution of wall pressure coefficient; (d) wall vorticity distribution

(a)

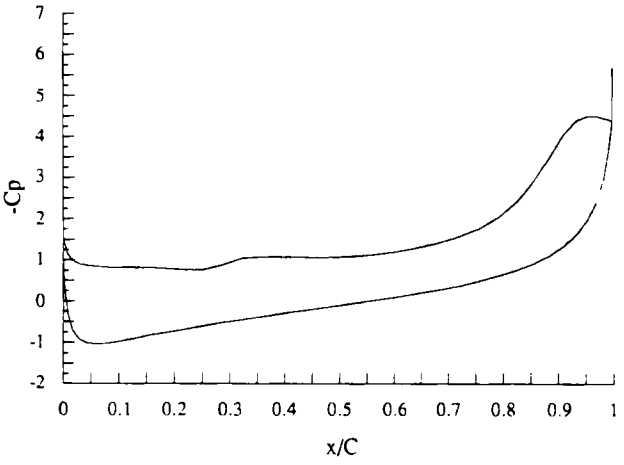


(c)

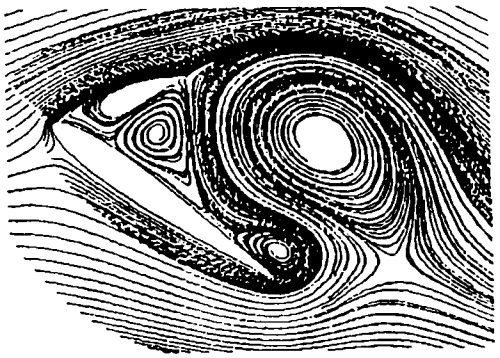

(b)

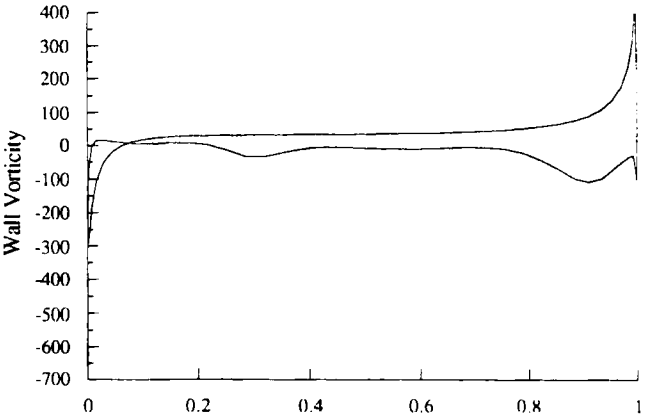


(d)

Figure 17. Impulsive start of aerofoil at $Re = 1000$, incidence 34 °, $t = 3{\cdot}2$: (a) visualization of path lines; (b) computed streamlines; (c) distribution of wall pressure coefficient; (d) wall vorticity distribution

(a)

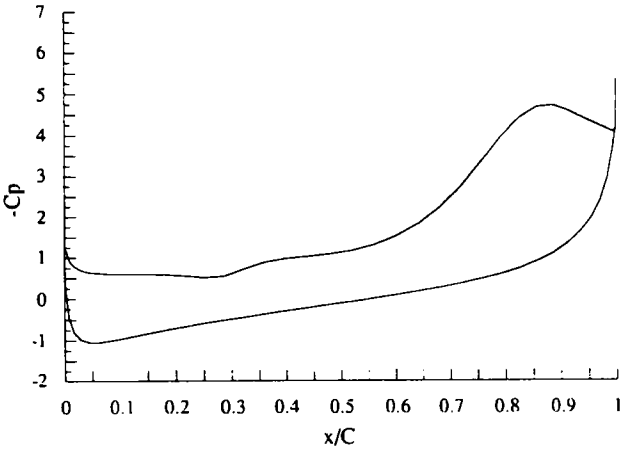


(c)

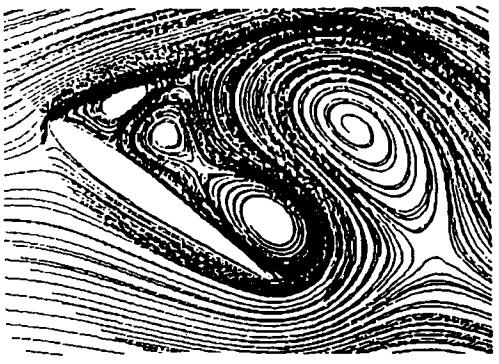

(b)

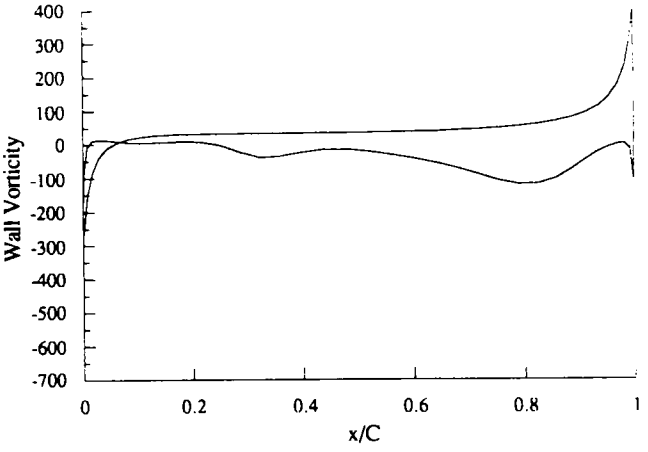


(d)

Figure 18. Impulsive start of aerofoil at $Re = 1000$, incidence 34 °, $t = 3{\cdot}6$: (a) visualization of path lines; (b) computed streamlines; (c) distribution of wall pressure coefficient; (d) wall vorticity distribution

(a)

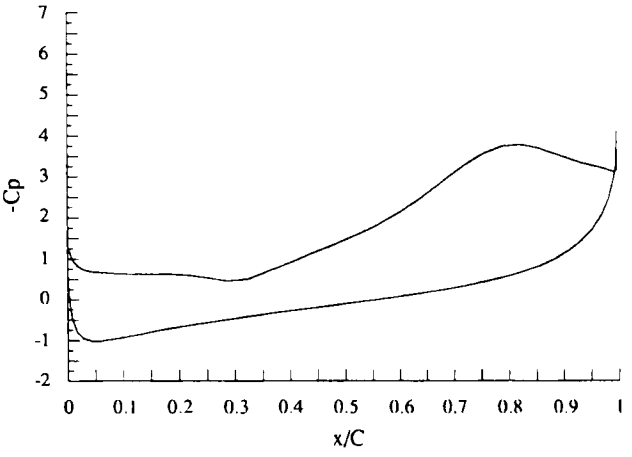


(c)

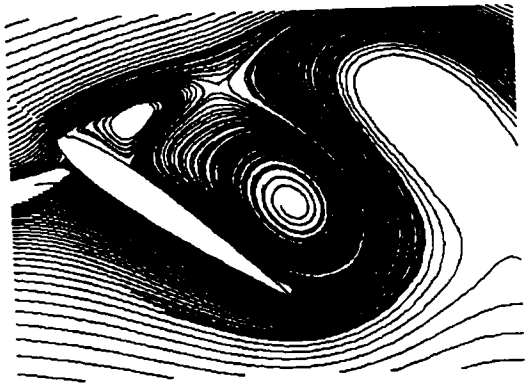

(b)

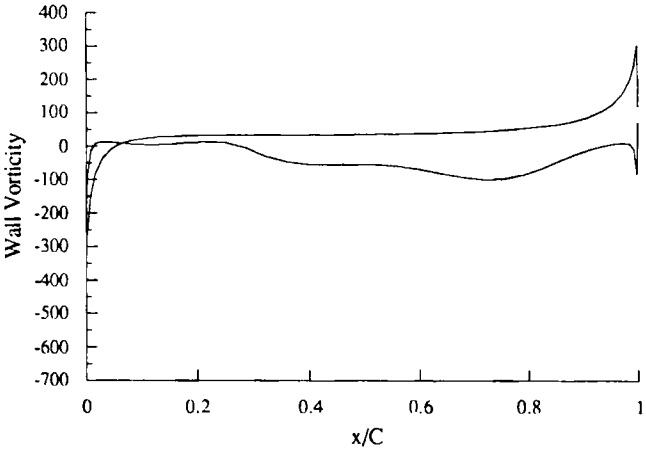


(d)

Figure 19. Impulsive start of aerofoil at $Re = 1000$, incidence 34°, $t = 4$: (a) visualization of pathlines; (b) computed streamlines; (c) distribution of wall pressure coefficient; (d) wall vorticity distribution

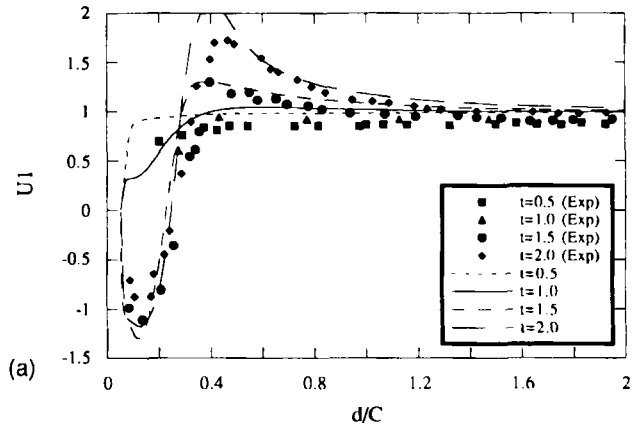


Figure 20. Impulsive start of aerofoil at $Re = 3000$, incidence 30 °, $t = 0{\cdot}5$, 1·0, 1·5, 2·0. Evolution with time of $\bar{U}_1$-velocity component along AA′ as a function of normalized distance to aerofoil. Comparisons between present calculations and experimental data[31]

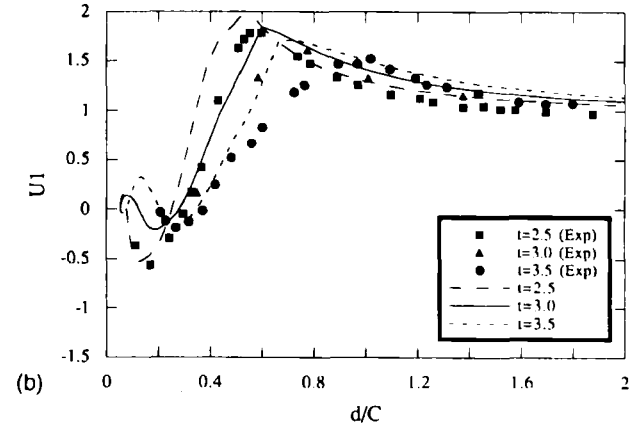


Figure 20(b). Impulsive start of aerofoil at $Re = 3000$, incidence 30 °, $t = 2{\cdot}5$, 3·0, 3·5. Evolution with time of $\bar{U}_1$-velocity component along AA′ as a function of normalized distance to aerofoil. Comparisons between present calculations and experimental data[31]

plotted (a) the visualization, (b) the set of computed streamlines, (c) the wall pressure coefficient and (d) the wall vorticity distribution. In the very first instants ($t < 0{\cdot}4$) after the impulsive start a small eddy is generated (Figures 14(a) and 14(b)). The stall phenomenon starts afterwards. First the vortex (a) develops on the upper part of the leading edge and moves along the upper surface of the aerofoil towards the trailing edge (Figures 15(a) and 15(b)). The development of the vortex (a) is easily seen from the distribution of the wall pressure coefficient presented in Figure 15(c) for corresponding time instants. In the second step a stable pair of secondary eddies (b) and (b′) develops at the leading edge while the main vortex (a) is still growing. The pair (b–b′) makes the pressure coefficient decrease and increases in size, since (b) is entrained while (b′) is fed with fluid from (a). In the third step the main vortex (a) is shed and a new eddy (c) appears at the trailing edge (Figures 16(a) and 16(b)), making the pressure coefficient increase again

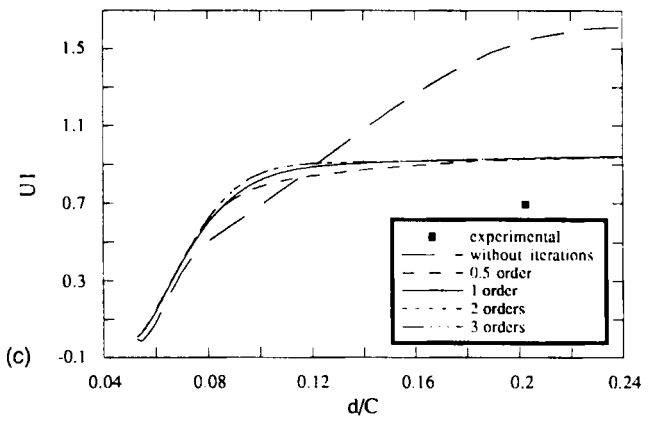


Figure 20(c). Impulsive start of aerofoil at $Re = 3000$, incidence 30 °, $t = 0{\cdot}5$, $dt = 0{\cdot}005$. Zoom of evolution with time of $\bar{U}_1$-velocity component along AA′ as a function of normalized distance to aerofoil. Influence of order of reduction of non-linear residuals (curves corresponding to two and three orders of residual reduction are identical)

(Figure 16(c)). The growth of the eddy (c) (Figure 17) raises the pressure coefficient and the eddy (b′) is absorbed by (c) as indicated in Figures 18 and 19. The other eddy (b) pushes (c) downstream. Finally, as (c) is shed, the pressure coefficient falls again. The Von Karman street is thus created.

*Case 2.* Case 2 is more difficult since the Reynolds number is higher. For this reason two grids have been considered: for the coarse grid which involves 80 × 60 points a time step $\Delta t = 0{\cdot}01$ is used; for the fine grid which involves 180 × 130 points a time step $\Delta t = 0{\cdot}005$ is used. Case 2 also allows a quantitative comparison up to $t = 3{\cdot}5$, since measurements of velocity profiles along the normal AA′ are also available in this case. The evolution with time of $\bar{U}_1$ and $\bar{U}_2$ along AA′ is presented in Figures 20 and 21 respectively. The results, which are completely grid-independent (and $\Delta t$-independent), show that the velocities are slightly over-estimated as in Case 1. It appears (Figure 20c) that on a given grid with a given time step

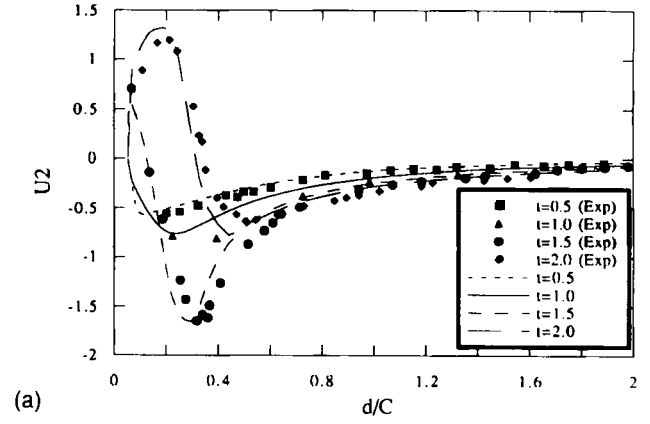


Figure 21(a). Impulsive start of aerofoil at $Re = 3000$, incidence 30 °, $t = 0{\cdot}5$, $1{\cdot}0$, $1{\cdot}5$, $2{\cdot}0$. Evolution with time of $\bar{U}_2$-velocity component along AA′ as a function of normalized distance to aerofoil. Comparisons between present calculations and experimental data[31]

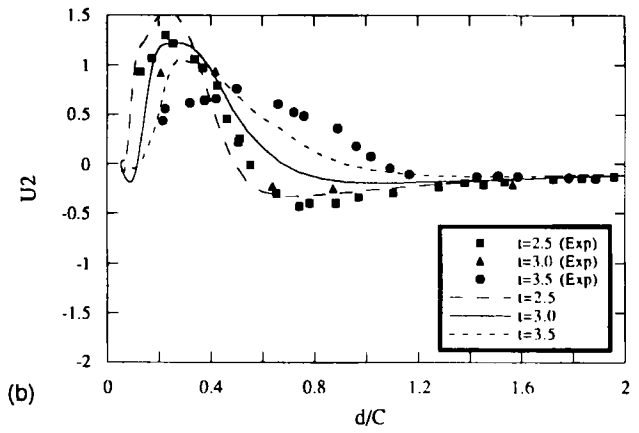


Figure 21(b). Impulsive start of aerofoil at $Re = 3000$, incidence 30°, $t = 2{\cdot}5, 3{\cdot}0, 3{\cdot}5$. Evolution with time of $\bar{U}_2$-velocity component along AA′ as a function of normalized distance to aerofoil. Comparisons between present calculations and experimental data[31]

non-linear iterations over $\mathbf{U}^*$ are required, since a linear extrapolation from $\mathbf{U}(t^0)$ and $\mathbf{U}(t^{00})$ leads to results noticeably different for $t < 0{\cdot}5$. A residual reduction by one order of magnitude is sufficient for $t < 0{\cdot}5$, where the flow evolves quite quickly. Moreover, for larger times Figures 20 and 21 indicate a shift between calculations and experiments: calculations lead experiments significantly, the grid-independent trend being especially apparent for $\bar{U}_2$.

## 5. CONCLUSIONS

We have presented an accurate and efficient primitive variable method for the solution of the Navier–Stokes equations in generalized co-ordinates on non-staggered grids. Through numerical tests we have shown that the method produces suitable results. The computed results, in good agreement with experimental data, demonstrate the ability of the method to compute highly unsteady flows such as the flow after an impulsive start.

## APPENDIX I

We present here the detailed form of equation (15) giving $\bar{U}_k(\mathrm{pN})$:

$$\bar{U}_k(\mathrm{pN}) = \frac{1}{e_1 + D_{\mathrm{pN}}} \{S_k(\mathrm{pN}) + [C^U_{\mathrm{NN}}\bar{U}_k(\mathrm{NN}) + C^U_{\mathrm{NP}}\bar{U}_k(\mathrm{NP}) + C^U_{\mathrm{PN}}\bar{U}_k(\mathrm{PN}) + C^U_{\mathrm{NM}}\bar{U}_k(\mathrm{NM}) + C^U_{\mathrm{MN}}\bar{U}_k(\mathrm{MN}) + C^U_{\mathrm{PP}}\bar{U}_k(\mathrm{PP})] + [C^{Pk}_{\mathrm{NN}}P(\mathrm{NN}) + C^{Pk}_{\mathrm{NP}}P(\mathrm{NP}) + C^{Pk}_{\mathrm{PN}}P(\mathrm{PN}) + C^{Pk}_{\mathrm{NM}}P(\mathrm{NM}) + C^{Pk}_{\mathrm{MN}}P(\mathrm{MN}) + C^{Pk}_{\mathrm{PP}}P(\mathrm{PP})]\}, \tag{30}$$

where $D_{\mathrm{pN}} = C_{\mathrm{N1}}(\mathrm{pN}) + C_{\mathrm{N2}}(\mathrm{pN})$ and $S_k(\mathrm{pN}) = -e_0\bar{U}^0_k(\mathrm{pN}) - e_{00}\bar{U}^{00}_k(\mathrm{pN})$ involves the known unsteady contributions. The second line of (30) specifies the summation over the velocity contributions at the set $NB(\mathrm{pN})$ of active nodes contributing to the flux at pN. The influence

coefficients resulting from the exponential scheme are given by

$$C^U_{NN} = -C_{M1}(pN), \quad C^U_{PN} = -C_{M2}(pN), \quad C^U_{NP} = -\tfrac{1}{2}C_{P2}(pN) - \tfrac{1}{4}d_{12}(pN),$$
$$C^U_{NM} = -\tfrac{1}{2}C_{M2}(pN) - \tfrac{1}{4}d_{12}(pN), \quad C^U_{PP} = -\tfrac{1}{2}C_{P2}(pN) + \tfrac{1}{4}d_{12}(pN),$$
$$C^U_{PM} = -\tfrac{1}{2}C_{M2}(pN) + \tfrac{1}{4}d_{12}(pN). \tag{31}$$

Equation (16a) is easily verified since

$$\sum_{NB(pN)} C^U_{NB(pN)} = -C_{M1}(pN) - C_{P1}(pN) - C_{M2}(pN) - C_{P2}(pN) = C_{P1}(pN) + C_{P2}(pN) \equiv D_{pN}.$$

The third line of (30) specifies the summation over the pressure contributions at the set $NB(pN)$ of active nodes contributing to the flux at pN. The corresponding influence coefficients from the exponential scheme are

$$C^{Pk}_{NP} = -C^{Pk}_{NN} = \tfrac{1}{2}a^1_k(pN), \quad C^{Pk}_{PP} = C^{Pk}_{NP} = -C^{Pk}_{PM} = C^{Pk}_{NM} = \tfrac{1}{4}a^2_k(pN) \tag{32}$$

and satisfy the consistency condition (16b),

$$\sum_{NB(PN)} C^{Pk}_{NB(pN)} = 0,$$

expressing that the pressure summation is of the gradient type. The same features are found if a hybrid scheme is used instead of the multiexponential scheme. For the sake of conciseness the relations (31) and (32) specifying the corresponding influence coefficients in (30) are omitted. The metric quantities in (31) and (32) are calculated from the knowledge of the set of points defining a grid which is twice as fine as the grid involving points O in Figure 1. The Peclet numbers, which are also required at point pN, are computed using a linear interpolation in the computational domain between nodal points NN and PN.

## APPENDIX II

The fully coupled system: the $ij$th block 3 × 3 row of **A** such that **AX** = **B** is

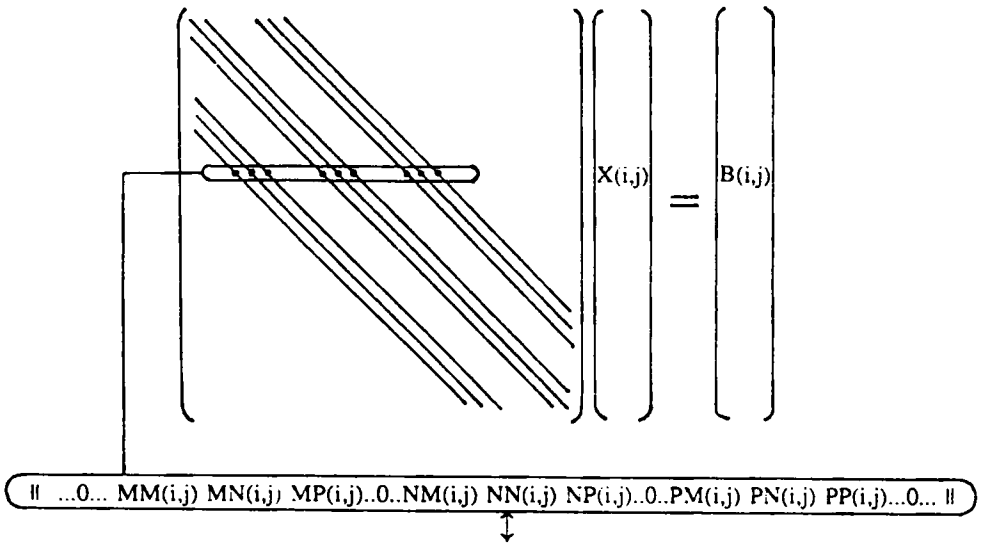

The diagonal block element corresponding to the element $\mathbf{X}(i, j)$ is

$$\mathrm{NN}(i, j) \equiv \begin{pmatrix} e_1 + D^U & 0 & -K_{\mathrm{NN}}^{1P} \\ 0 & e_1 + D^U & -K_{\mathrm{NN}}^{2P} \\ K_{\mathrm{NN}}^{P1} & K_{\mathrm{NN}}^{P2} & K_{\mathrm{NN}}^{PP} \end{pmatrix} (i, j).$$

The block element corresponding to the unknown $\mathbf{X}(i, j+1)$ is

$$\mathrm{NP}(i, j) \equiv \begin{pmatrix} -K_{\mathrm{NP}}^{U} & 0 & -K_{\mathrm{NP}}^{1P} \\ 0 & -K_{\mathrm{NP}}^{U} & -K_{\mathrm{NP}}^{2P} \\ K_{\mathrm{NP}}^{P1} & K_{\mathrm{NP}}^{P2} & K_{\mathrm{NP}}^{PP} \end{pmatrix} (i, j).$$

The right-hand side corresponding to the known vector $\mathbf{B}(i, j)$ is

$$\mathbf{B}(i, j) \equiv \| \Sigma_1 \Sigma_2 \Sigma_P \|^T (i, j).$$

## REFERENCES


1. R. Peyret and T. D. Taylor, *Computational Methods for Fluid Flow*, Springer, New York, 1983.
2. B. J. Alfrink, 'On the Neuman problem for the pressure in Navier–Stokes model', in C. Taylor and B. A. Schrefler (eds), *Proc. 2nd. Int. Conf. on Numerical Methods in Laminar and Turbulent Flows*, Pineridge, Swansea, 1981, pp. 389–401.
3. S. Abdallah, 'Numerical solutions for the pressure Poisson equation with Neuman boundary conditions using a non-staggered grid, I', *J. Comput. Phys.*, **70**, 182–192 (1987).
4. J. Piquet and M. Visonneau, 'Computation of the flow past shiplike hulls', *Comput. Fluids*, **19**, 183–215 (1991).
5. M. Rosenfeld, D. Kwak and M. Vinokur, 'A fractional step solution method for the time-accurate incompressible Navier–Stokes equations in generalized coordinate systems', *J. Comput. Phys.*, **94**, 102–137 (1991).
6. T. Isogahi, B. R. Shin and H. Daiguji, 'Application of an implicit time-machine scheme to a three-dimensional incompressible flow problem in curvilinear coordinate systems', *Comput. Fluids*, **21**, 163–175 (1992).
7. C. M. Rhie and W. L. Chow, 'Numerical study of the turbulent flow past an airfoil with trailing edge separation', *AIAA J.*, **21**, 1525–1532 (1983).
8. G. E. Schneider and M. J. Raw, 'Control-volume finite element method for heat transfer and fluid flow using colocated variables', *Numer. Heat Transfer*, **11**, 363–400 (1987).
9. A. S. Dvinsky and J. K. Dukowicz, 'Null-space-free methods for the incompressible Navier–Stokes equations on non-staggered curvilinear grids', *Comput. Fluids*, **22**, 685–696 (1993).
10. R. I. Issa, 'Solution of the implicitly discretized fluid equations by operator-splitting', *J. Comput. Phys.*, **62**, 40–65 (1985).
11. Y. Lecointe and J. Piquet, 'Compact finite-difference methods for solving incompressible Navier–Stokes equations around oscillating bodies', *VKI-LS 1985-04*, 1985.
12. Ta Phuoc Loc and R. Bouard, 'Numerical solution of the early stage of the unsteady viscous flow around a circular cylinder: a comparison between experimental visualization and measurements', *J. Fluid Mech.*, **160**, 93–117 (1985).
13. R. Bouard and M. Coutanceau, 'The early stages of development of the wake behind an impulsively started cylinder for $40 < Re < 10^4$', *J. Fluid Mech.*, **101**, 583–607 (1980).
14. D. P. Telionis, *Unsteady Viscous Flow*, Springer, New York, 1981.
15. U. B. Mehta and Z. Lavan, 'Starting vortex, separation bubbles and stall: a numerical study of laminar unsteady flow around an airfoil', *J. Fluid Mech.*, **67**, 227–256 (1975).
16. U. B. Mehta, 'Dynamic stall of an oscillating airfoil', *AGARD CP 227*, 1977, Paper 23.
17. Y. Lecointe and J. Piquet, 'Unsteady viscous flow round circular cylinders and airfoils', *AIAA Paper 85-1490*, 1985.
18. I. V. Zeleznov and V. Ya. Shkadov, 'Viscous flow past an airfoil', *Fluid Dyn.*, **4**, 531–537 (1987).
19. L. Mane, Ta Phuoc Loc and H. Werlé, 'Sur le décollement instationnaire autour d'un profil à grands nombres de Reynolds: une comparaison calcul-expérience', *C. R. Acad. Sci. Paris II*, **305**, 229–232 (1987).
20. K. Ohmi, M. Coutanceau, Ta Phuoc Loc and A. Dulieu, 'Vortex formation around an oscillating and translating airfoil at large incidences', *J. Fluid Mech.*, **211**, 37–60 (1990).
21. K. Ohmi, M. Coutanceau, O. Daube and Ta Phuoc Loc, 'Further experiments on vortex formation around an oscillating and translating airfoil at large incidences', *J. Fluid Mech.*, **225**, 607–630 (1991).
22. J. C. Wu, S. Sampath and N. L. Sankar, 'A numerical study of unsteady viscous flows around airfoils', *AGARD CP227*, 1977, Paper 24.
23. J. C. Wu and A. Sugavanam, 'A method for the numerical solution of turbulent flow problems', *AIAA J.*, **16**, 948–955 (1978).

24. I. H. Tuncer, J. C. Wu and C. M. Wang, 'Theoretical and numerical studies of oscillating airfoils', *AIAA J.*, **28**, 1615–1624 (1990).
25. S. J. Shamroth and H. J. Gibeling, 'The prediction of the turbulent flow field about an isolated airfoil', *AIAA Paper 79-1543*, 1979.
26. N. L. Sankar and Y. Tassa, 'Reynolds number and stability effects on dynamic stall of a NACA0012 airfoil', *AIAA Paper 80-0010*, 1980.
27. H. Hegna, 'Numerical solution of incompressible turbulent flow over airfoils near stall', *AIAA J.*, **20**, 29–30 (1982).
28. G. Tzabiras, A. Dimas and T. Loukakis, 'A numerical method for the calculation of incompressible, steady, separated flows around aerofoils', *Int. j. numer. methods fluids*, **6**, 789–809 (1986).
29. S. Ogawa and T. Ishiguro, 'A method for computing flow fields around moving bodies', *J. Comput. Phys.*, **69**, 49–68 (1987).
30. S. Mittal and T. E. Tezduyar, 'A finite element study of incompressible flows past oscillating cylinders and aerofoils', *Int. j. numer. methods fluids*, **15**, 1073–1118 (1992).
31. O. Daube, Ta Phuoc Loc, P. Monnet and M. Coutanceau, 'Ecoulement instationnaire décollé d'un fluide incompressible autour d'un profil: une comparaison théorie–expérience', *AGARD CP 386*, 1985, Paper 3.
32. M. F. Collin, M. Coutanceau, A. Texier, A. Dulieu and Ta Phuoc Loc, 'Analyse automatique de clichés de visualisations d'écoulements', *DRET Contract Rep. 87/212*, 1990.